Gyrokinetic simulations for turbulent transport of multi-ion-species plasmas in helical systems

Gyrokinetic simulations for turbulent transport of multi-ion-species plasmas in helical systems

M. Nunami,[1,2,a)] M. Nakata,[1,2] S. Toda,[1,2] and H. Sugama[1,2]
[1)] *National Institute for Fusion Science / National Institutes of Natural Sciences, Toki, Gifu 509-5292, Japan*
[2)] *The Graduate University for Advanced Studies, SOKENDAI, Toki, Gifu 509-5292, Japan*

(Dated: 9 April 2020)

The turbulent transport of the magnetic confinement plasmas including multi-ion-particle-species in helical systems such as Large Helical Device (LHD) [Y. Takeiri, *et al.*, Nucl. Fusion **57**, 102023 (2017)] and their plasma profile sensitivities are investigated by the local flux-tube gyrokinetic simulations. In the multi-ion-species plasmas, while the heat transport of each particle species has slightly different sensitivity on the plasma temperature gradients and the density gradients, there exist quite different dependencies in the particle transport on the radial gradient profiles of the plasma temperatures and densities between each particle species. Furthermore, in the LHD plasma with the carbon impurity hole structure [K. Ida, *et al.*, Plasma Phys. **16**, 056111 (2009)], the turbulent particle transport flux of the impurity carbon ion remains radially inward-directed robustly within the wide ranges of the radial gradient profiles of the plasma temperatures and densities.

Keywords: Turbulent transport, Profile sensitivity, Large Helical Device, Impurity hole

I. INTRODUCTION

Understanding the physical mechanism for the plasma turbulent transport phenomena is one of the most critical issues in the magnetically confined fusion researches because the turbulent transport often strongly influences the plasma confinement performance in the fusion reactors. The turbulent transport is considered to be driven by micro-instabilities such as ion temperature gradient (ITG) mode.[1] The numerical simulations based on the gyrokinetic approaches are useful and powerful for analyzing the turbulent transport physics. Due to the recent rapid progress of the large-scale simulations using the high-performance computers, it is possible to validate the gyrokinetic simulation results against the experimental observations for the plasma temperature and density profiles with the experimental errors considered[2]. For predicting the performances of the burning plasmas in the ITER, future fusion reactors, and also Stellarator/Heliotron systems such as the Wendelstein 7-X[3] and the Large Helical Device (LHD)[4], the understanding of the turbulent transport physics of the multi-ion-species plasma is strongly demanded because the realistic plasmas generally consist of multi-ion-species.

In our linear gyrokinetic analyses for the multi-ion-species plasmas in LHD, it was confirmed that the linear growth rate of the microinstability strongly depends on the relative densities and temperature profiles of each species[5,6], while the large density of the impurity ions with higher electric charge causes the dilution of the main hydrogen ion which is the main driver of the instability. This means that the details of the plasma profiles for each particle species can affect the resultant transport levels of the multi-ion-species plasmas. In the global gyrokinetic simulation study[7], it has been also confirmed that the impurity ions can reduce the turbulent transport driven by ion temperature gradient. The impurity ions are often accumulated in core regions, and the accumulated impurities degrade confinement performance of the plasmas by radiation losses of heat, reduction of the plasma temperature, and other confirmed reasons. On the other hand, in the LHD plasmas heated by neutral beam injection (NBI), we often observe the extremely hollow impurity density profiles called impurity hole[8] with the internal transport barriers. Therefore, the clarification of the generation mechanism of the impurity hole is a critical issue for achieving the high-performance of magnetically confined plasmas.

Now, we consider a simple equation of continuity for the densities n_s of the species s in such plasmas,

$$\frac{\partial n_s(\rho)}{\partial t} + \frac{1}{V'}\frac{\partial}{\partial \rho} V' \left(\Gamma_s^{(\mathrm{Trb})}(\rho) + \Gamma_s^{(\mathrm{NC})}(\rho) \right) = \mathcal{S}_s, \quad (1)$$

with the given particle source term $\mathcal{S}_s$. Here, ρ is the normalized radial positions, V is the volume surrounded by the flux-surface labeled by ρ, V' means radial derivatives of V, and $\Gamma_s^{(\mathrm{Trb})}(\rho)$ and $\Gamma_s^{(\mathrm{NC})}(\rho)$ are the turbulent and neoclassical contributions of the particle transport fluxes of the species s, respectively. In Eq.(1), if the system is in the steady state, i.e., $\partial n_s/\partial t = 0$, and the particle source term can be neglected, $\mathcal{S}_s = 0$, the total particle transport fluxes $\Gamma_s^{(\mathrm{Total})}(\rho) = \Gamma_s^{(\mathrm{Trb})}(\rho) + \Gamma_s^{(\mathrm{NC})}(\rho)$ should vanish for each species. In our recent work for the neoclassical transport analyses[9] for the LHD impurity hole plasma, the neoclassical contribution of the impurity carbon particle transport can be radially outward-directed. According to the neoclassical estimates, if the sufficient external torque by the NBI heating exists, the

[a)] nunami.masanori@nifs.ac.jp

radial electric field which satisfies the ambipolar condition, $\Gamma_{\rm e}^{\rm (NC)} = \sum_{s\neq {\rm e}} Z_s \Gamma_s^{\rm (NC)}$, can be positive, i.e., the plasma can be in the "electron root" regime at radii where the impurity hole structure is generated. Here, Z_s is the charge number of the species s. In the case of the "electron root," the neoclassical particle transport flux of the impurity carbon can be radially outward-directed. Therefore, for the particle balance between the turbulent and neoclassical contributions, we must confirm that the turbulent contributions of the particle transport will be radially inward-directed. Indeed, the quasi-linear analyses of the turbulent transport of the impurity ions in the LHD impurity hole plasma indicated that the quasi-linear particle fluxes of the carbon impurity are radially inward-directed[6]. In this work, in order to understand the turbulent transport of the multi-ion-species plasmas including the impurity ions, and to clarify the turbulent contributions in the transport phenomena, we perform the gyrokinetic simulations for the transport of the multi-ion-species LHD plasmas with the impurity hole structure.

This paper is organized as follows. In Sec. II, the LHD plasma with the impurity hole structure is briefly reviewed. In Sec. III, we describe the simulation model used in the present study and basic equations employed in the calculations. In Sec. IV, we show the linear instability analyses and the nonlinear simulation results for the turbulent transport. And we evaluate the turbulent contributions of the heat and particle transport. In Sec. V, we compare the turbulent contributions and the neoclassical contributions for the multi-species plasma transport. Finally, we summarize the work in Sec. VI.

II. IMPURITY HOLE PLASMA IN LHD

In the LHD experiment with high ion temperature heated by the NBI, we often observe the extremely hollow impurity density profile which is called impurity hole with the internal transport barriers. In a typical case of the LHD impurity hole plasma of the shot number #113208 at $t = 4.64$s, which is the same plasma discussed in the neoclassical analyses[9] and the quasi-linear analyses[6]. Fig. 1 shows the radial profiles for temperatures T_s, the radial gradients of the temperatures R_0/L_{Ts}, the densities n_s, the normalized charge densities f_{Cs}, the radial gradients of the densities R_0/L_{ns}, and $f_{Cs}R_0/L_{ns}$. Here, R_0 is the major radius, L_{Ts} is the temperature gradient scale length for the species s defined by $L_{Ts}^{-1} \equiv -d\ln T_s/dr$, L_{ns} is the density gradient scale length for the species s defined by $L_{ns}^{-1} \equiv -d\ln n_s/dr$, and f_{Cs} is the normalized charge density for the ion species s defined by $f_{Cs} \equiv n_s Z_s/n_{\rm e}$. In this plasma, there are four particle species including electron e^-, hydrogen ion H^+, helium ion He^{2+}, and carbon ion C^{6+}. The temperature for each ion species is assumed to be the same with each other. As shown in Fig.1(c) and (e), the impurity carbon density has strong hollow structure for the inner radial region around $\rho \sim 0.4$ to 0.7. While there are several structures of the radial profiles of the densities between each species, the quasi-neutrality conditions, $f_{Ce} = \sum_{s\neq e} f_{Cs}$ and $f_{Ce}/L_{ne} = \sum_{s\neq e} f_{Cs}/L_{ns}$, are exactly satisfied as shown in Fig.1(d) and (f). In the following sections, we will analyze the turbulent transport in this plasma by utilizing the gyrokinetic simulations.

III. GYROKINETIC SIMULATION MODEL

In this paper, in order to evaluate the turbulent transport of the multi-species helical plasmas, we employ the local δf flux-tube gyrokinetic code, GKV[10–13]. The code can solve the time evolution of the wavenumber-space representation of the gyrokinetic equation for the perturbed gyrocenter distribution function of species s in the three-dimensional equilibrium field. The perturbed distribution function is represented by $\delta f_{sk_\perp} = -e_s J_{0s}\delta\phi_{k_\perp} F_{{\rm M}s}/T_s + h_{sk_\perp}$, where $h_{sk_\perp}$ is the non-adiabatic part of the perturbed distribution function. The gyrokinetic equation for $h_{sk_\perp}$ is represented by

$$\left(\frac{\partial}{\partial t} + v_\parallel \boldsymbol{b}\cdot\nabla + i\omega_{{\rm D}s} - \frac{\mu \boldsymbol{b}\cdot\nabla B}{m_s}\frac{\partial}{\partial v_\parallel}\right) h_{sk_\perp} - \frac{c}{B}\sum_{\Delta} \boldsymbol{b}\cdot(\boldsymbol{k}'_\perp \times \boldsymbol{k}''_\perp)\delta\Psi_{k'_\perp} h_{sk''_\perp} = \frac{e_s F_{{\rm M}s}}{T_s}\left(\frac{\partial}{\partial t} + i\omega_{*Ts}\right)\delta\Psi_{k_\perp} + C_s(h_{sk_\perp}), \quad (2)$$

where m_s, e_s, and T_s are the particle mass, the electric charge, and the equilibrium temperature of the particle species s, respectively. As the velocity space coordinates, the magnetic moment $\mu = v_\perp^2/2B$ and the parallel velocity $v_\parallel$ are employed. $\delta\Psi_{k_\perp} = J_{0s}[\delta\phi_{k_\perp} - (v_\parallel/c)\delta A_{\parallel k_\perp}]$ is the gyro-averaged potential fluctuation with the zeroth order Bessel function $J_{0s} = J_0(k_\perp v_\perp/\Omega_s)$ and $\Omega_s = e_s B/(m_s c)$ is the gyrofrequency of the particle species s. And $\omega_{{\rm D}s} = \boldsymbol{k}_\perp \cdot \boldsymbol{v}_{s{\rm D}}$ and $\omega_{*Ts} = \boldsymbol{k}_\perp \cdot \boldsymbol{v}_{s*}$ are the magnetic and the diamagnetic drift frequencies with $\boldsymbol{v}_{s{\rm D}} = (c/e_s B)\boldsymbol{b}\times(\mu\nabla B + m_s v_\parallel^2 \boldsymbol{b}\cdot\nabla\boldsymbol{b})$ and $\boldsymbol{v}_{s*} = (cT_s/e_s B)\boldsymbol{b}\times[\nabla\ln n_s + (m_s v^2/2T_s - 3/2)\nabla\ln T_s]$, respectively. A linearized model collision operator C_s is introduced using a simplified Lenard-Bernstein type model[14] for the numerical scans for wide parameter regimes. In Eq.(2), the symbol $\sum_\Delta$ represents double summations with respect to $\boldsymbol{k}'_\perp$ and $\boldsymbol{k}''_\perp$, satisfying $\boldsymbol{k}_\perp = \boldsymbol{k}'_\perp + \boldsymbol{k}''_\perp$. The equation is solved in the local flux-tube coordinates, $\{x, y, z\} = \{a(\rho-\rho_0), a\rho_0 q(\rho_0)^{-1}[q(\rho)\theta - \zeta], \theta\}$ with conventional flux-coordinate system $\{\rho, \theta, \zeta\}$. Here, a is the minor radius, and $q(\rho_0)$ is the safety factor at the focused magnetic flux surface labeled by ρ_0, and $\rho \equiv \sqrt{\psi/\psi_{\rm a}}$ is the normalized radial coordinate. And ψ represents the toroidal magnetic flux, and $\psi_{\rm a}$ is also defined by the value at the last closed surface. The fluctuations of the poten-

tials are calculated by the Poisson and Ampère equations,

$$\left(k_\perp^2 + \lambda_{\rm D}^{-2}\right)\delta\phi_{k_\perp} = 4\pi\sum_s e_s \int d\boldsymbol{v} J_{0s} h_{sk_\perp}, \qquad (3)$$

$$k_\perp^2 \delta A_{\parallel k_\perp} = \frac{4\pi}{c}\sum_s e_s \int d\boldsymbol{v} v_\parallel J_{0s} h_{sk_\perp}. \qquad (4)$$

Here, $\lambda_{\rm D}$ is the Debye length.

IV. TURBULENT TRANSPORT ANALYSES IN LHD IMPURITY HOLE PLASMA

A. Linear analyses for microinstabilities

In this subsection, before the nonlinear turbulence simulation analyses, the results of the linear gyrokinetic analyses are introduced. For the analyses of the microinstabilities in the LHD impurity hole plasma #113208 at $t = 4.64$s, we performed linear gyrokinetic simulations. In the plasma, the plasma is in the neoclassical regime of $1/\nu$ or $\sqrt{\nu}$ for the bulk ions and the electron, and around the boundary of the banana and the plateau regimes for the carbon ion where the normalized collision frequencies are shown in Table I. In Fig.2, the poloidal wavenumber spectra of linear growth rates and the real frequencies of the micro-instabilities at $\rho = 0.42,\ 0.52,\ 0.61$, and 0.70 in the LHD impurity hole plasma are obtained from electromagnetic linear gyrokinetic simulations with the typical value of local beta in the plasma, $\beta = 0.5\%$. Here, $\rho_{\rm H}$ is the thermal gyroradius and $v_{\rm tH}$ is the thermal speed of the hydrogen ion. In this plasma, we found that the ITG modes with negative real frequency are most unstable. As seen in the figure, the ITG modes are unstable enough anywhere the strong hollow density structure of the impurity carbon ion exists, $0.4 \lesssim \rho \lesssim 0.7$. Furthermore, for changing the density gradients of the carbon ion $L_{n\rm C}^{(\rm nom)}/L_{n\rm C}$, it is found that the instability channel does not change, namely, the ITG modes are still dominant instability. Here, the nominal values of the density gradient length $L_{n\rm C}^{(\rm nom)}$ will be shown in Table III. According to the previous paper[6] on the quasi-linear gyrokinetic analyses, the quasi-linear particle transport flux of the carbon ion based on the linear gyrokinetic simulations, $\Gamma_C^{(\rm QL)} \equiv \left(\Gamma_C^{(\rm lin)}(n_{\rm e}/n_{\rm C})/\langle|\delta\phi|^2\rangle\right)\left(\gamma/(k_y\rho_{\rm H})^2\right)$, should be negative, i.e., radially inward-directed as long as the hollow density profile remains.

B. Turbulent heat transport

In many gyrokinetic simulations performed to date, a significant fact has been found. That is, the plasma near the marginal gradients of the plasma temperature and density have the strong stiffness of the temperature and density profiles against the turbulent transport fluxes[15–19], where it has been considered that such strong stiffness is significant for investigating the underestimation of the ion heat transport, namely, the transport shortfall.[20,21] Therefore, in terms of the validation metrics[22] of the simulations against the experiments, to clarify the turbulent contributions of the transport of the multi-species plasma, we should analyze the sensitivity of the turbulent transport of heat and particle to the radial gradients of the plasma temperatures and densities for wide ranges.

TABLE I. The normalized collision frequencies $\nu_{ab}^* \equiv q_0 R_0 \tau_{ab}^{-1}/(\sqrt{2}\epsilon^{3/2} v_{ta})$ used in the simulations at $\rho = 0.61$. Here, τ_{ab}^{-1} is the characteristic collision time between species a and b, and ϵ is the inverse aspect ratio.

a b	ν_{ab}^*	a b	ν_{ab}^*
e e	3.23×10^{-2}	He e	8.95×10^{-2}
e H	1.64×10^{-2}	He H	5.21×10^{-2}
e He	2.21×10^{-2}	He He	6.72×10^{-2}
e C	2.91×10^{-2}	He C	8.29×10^{-2}
H e	2.23×10^{-2}	C e	0.81×10^{0}
H H	1.36×10^{-2}	C H	0.44×10^{0}
H He	1.75×10^{-2}	C He	0.57×10^{0}
H C	2.16×10^{-2}	C C	0.70×10^{0}

In this subsection, first, we estimate the sensitivity of the turbulent heat transport to the plasma temperature gradients and density gradients by the nonlinear gyrokinetic turbulence simulations using the GKV code. Here, to reduce the computational costs, we employed the following model LHD configuration with limited numbers of field components from the field configuration obtained by the three-dimensional equilibrium code VMEC[23],

$$B = B_0\Bigg[1 - \epsilon_{00}(\rho) - \epsilon_{\rm t}(\rho)\cos\theta - \sum_{l=L-1}^{L+1}\epsilon_l(\rho)\cos\left[l\theta - M\zeta\right]\Bigg], \qquad (5)$$

where θ is the poloidal angle, ζ is the toroidal angle in the magnetic coordinate system $\{\rho, \theta, \zeta\}$, $\epsilon_{\rm t}$ and $\epsilon_{\rm h} = \epsilon_L$ are the toroidal and the main helicities, respectively. And $\epsilon_+ = \epsilon_{L+1}$ and $\epsilon_- = \epsilon_{L-1}$ are two side-band helical components. M and L indicate the main period numbers of the confinement field in the toroidal and poloidal directions, respectively. For the LHD, $L = 2$ and $M = 10$ should be employed. In Table II, the parameters are summarized, which are obtained from the VMEC configuration in terms of the toroidal, main helical, two side-band components, and their radial derivatives. Here, the model configuration does not affect the main features of the transport[11]. The number of the grid points in the phase space $(x, y, z, v_\parallel, \mu)$ used in the simulations is $256 \times 96 \times 256 \times 64 \times 16$. In the real space, we employ $-\pi \le z < \pi$ along the field line, the system lengths in the perpendicular directions are $L_x = 2\pi/\Delta k_x$ and $L_y = 2\pi/\Delta k_y$ with the minimum wavenumbers

TABLE II. Parameters at the flux surface $\rho = 0.61$ employed in the GKV code. The prime symbol means $A' = dA/d\rho$.

q_0	r_0/R_0	$\epsilon_{\rm t}$	$\epsilon_{\rm h}/\epsilon_{\rm t}$	$\epsilon_-/\epsilon_{\rm t}$	$\epsilon_+/\epsilon_{\rm t}$
1.6	0.1019	0.08996	0.9745	-0.5074	0.1294
$\hat{s}$	$\rho_0\epsilon'_{00}/\epsilon_{\rm t}$	$\rho_0\epsilon'_{\rm t}/\epsilon_{\rm t}$	$\rho_0\epsilon'_{\rm h}/\epsilon_{\rm t}$	$\rho_0\epsilon'_-/\epsilon_{\rm t}$	$\rho_0\epsilon'_+/\epsilon_{\rm t}$
-0.8672	0.1294	0.9970	2.1603	-1.1041	0.1163

TABLE III. Nominal values of the radial gradients of the temperature and densities at $\rho = 0.61$ employed in the nonlinear simulations.

$R_0/L_{T\rm e}^{(\rm nom)}$	$R_0/L_{T\rm i}^{(\rm nom)}$	$R_0/L_{n\rm e}^{(\rm nom)}$
7.6485	13.3487	-2.38929
$R_0/L_{n\rm H}^{(\rm nom)}$	$R_0/L_{n\rm He}^{(\rm nom)}$	$R_0/L_{n\rm C}^{(\rm nom)}$
-0.8228	-0.8228	-10.6738

$(\Delta k_x\rho_{\rm H}, \Delta k_y\rho_{\rm H}) = (0.109, 0.080)$. In the velocity space, the simulation box size is $-4.5v_{\rm tH} \le v_\parallel \le 4.5v_{\rm tH}$ and $0 \le \mu \le 10.13 m_{\rm H} v_{\rm tH}^2/B$.

Figure 3 shows the time evolutions of the heat fluxes and the particle fluxes at $\rho = 0.61$ where the strong impurity hole is generated with the nominal values of the temperature and density gradients shown in Table III. For $t > 50R_0/v_{\rm tH}$, it is confirmed that the turbulences are sufficiently saturated with well developed zonal flows. Figures 4 show the dependences of the turbulent heat transport fluxes for all four species on the electron and the ion temperature gradient lengths at $\rho = 0.61$. In the figures, we performed 25 nonlinear gyrokinetic simulations with changing the temperature gradients of ion and electron from $0.6 \times R_0/L_{T\rm i,e}^{(\rm nom)}$ to $1.5 \times R_0/L_{T\rm i,e}^{(\rm nom)}$, where $R_0/L_{T\rm i,e}^{(\rm nom)}$ are the nominal values of the temperature gradients shown in Table III. All ion heat fluxes rapidly increase with increasing the ion temperature gradient, which is a typical property of the ITG-driven turbulent transport, where the electron heat flux also depends on the electron temperature gradient. As shown in Fig.4, the experimental values of the anomalous contributions of the heat fluxes $Q_s^{(\rm ano)}$ for $s =$ e, H, and He are within the scan ranges of the temperature gradients performed in the simulations. For the carbon heat flux and the particle fluxes of all species, we could not discuss the validations of the simulations because the experimental data for them are not sufficiently available. In the simulations, the electromagnetic contributions in the heat fluxes are relatively small compared with the electrostatic contributions, $Q_s^{(\rm EM)}/Q_s^{(\rm Total)} < 1\%$. On the other hand, Fig.5 shows the dependences of the turbulent heat transport fluxes on the density gradients. Here, to concentrate on the responses of the heat fluxes to the density gradient changing, the radial gradient of the density for specific species is artificially changing with other fixed species density gradients. In the figure, we performed a total of 28 nonlinear gyrokinetic simulations with changing the density gradients. From the figure, there are small differences between each species in the dependences on the density gradients. Therefore, in the turbulent heat transport, there are slight differences of the plasma gradient profile dependences between each particle species due to the turbulent potential fluctuation which is shared with all species.

C. Turbulent particle transport

In this subsection, we estimate the sensitivity of the turbulent particle transport to the plasma temperature gradients and density gradients by the nonlinear gyrokinetic turbulence simulations.

Figure 6 shows the dependences of the turbulent particle transport fluxes for all four species on electron and ion temperature gradient lengths at $\rho = 0.61$, where the strong hollow density profile of the impurity carbon exists. Here, the turbulent particle fluxes satisfy the ambi-polar condition at each gradient. In contrast to the cases of the heat transport fluxes in Fig.4, as seen in Fig.6, there are quite different temperature gradient dependences of the particle fluxes among different particle species. For example, if the ion temperature gradient increases, the particle transport fluxes for the hydrogen and the helium ions increase while the particle fluxes of the electron and the carbon ion decrease. Furthermore, if the electron temperature gradient increases, all particle fluxes decrease. For the hydrogen ion, especially, the direction of the particle flux can be changed from positive for higher grad-$T_{\rm i}$ and lower grad-$T_{\rm e}$ to negative for lower grad-$T_{\rm i}$ and higher grad-$T_{\rm e}$. Since the ambi-polar condition $\Gamma_{\rm e}^{(\rm Trb)} = \sum_{s\neq {\rm e}} Z_s \Gamma_s^{(\rm Trb)}$ is satisfied[24] at each gradient, such complicated dependences on the temperature gradients should be determined by the balances of the particle fluxes between each species. In addition to these complicated temperature gradient dependences, in wide ranges over 50% changes of the ion and the electron temperature gradients from their nominal values which are shown in Table III, the impurity carbon particle flux remains negative. Therefore, the turbulent particle flux of the carbon impurity is radially inward-directed, while the turbulent particle flux of the helium ion remains outward-directed. In the wavenumber spectra of the particle fluxes shown in Fig.7, it is found that the spectra of the particle fluxes have a peak near the wavenumber where the ITG mode is most unstable as shown in Fig.2.

On the other hand, particle fluxes are strongly affected by not only the temperature gradients as shown in Fig.6 but also the density gradient lengths for several particle species. Figure 8 shows the dependences of the turbulent particle transport fluxes on the density gradients. Here, the density gradient length dependences of turbulent particle fluxes are evaluated by the nonlinear gy-

rokinetic simulations by changing the density gradients for specific species with other fixed species density gradients. In Fig.8, we can see that the ambi-polar condition is certainly satisfied in whole regions of the density gradients. Furthermore, compared with the cases of the heat transport flux, there are quite different dependences on the density gradients. For changing density gradients of bulk ions shown in Fig.8(b) and (c), there seems to be clear balance relations between the pair of hydrogen and helium ions and the pair of electron and carbon ion. Since it is still not clear whether the balance relations are accidental or not, we should perform more precise theoretical analyses, e.g., quasi-linear analyses as future works. On the other hand, for changing density gradients of electron and carbon ion shown in Fig.8(a) and (d), there are still complicated dependences without the clear relation found in the cases of changing density gradients of bulk ions. However, the carbon particle flux should not be radially outward-directed unless the impurity hole structure disappears, i.e., the turbulent particle transport of the carbon ion can be outward-directed only when the carbon density profile is sufficiently peaked. Therefore, at least in the results obtained here, the turbulent particle transport of the impurity carbon ion in the impurity hole plasma is radially inward-directed. This conclusion is consistent with our previous quasi-linear estimates for the impurity carbon particle transport[6]. Therefore, if the system is in the steady state with negligible auxiliary particle sources or sinks, the neoclassical carbon particle flux should be expected to be outward-directed against the inward-directed turbulent flux.

V. AGAINST NEOCLASSICAL CONTRIBUTION OF PARTICLE TRANSPORT

For the balance relation between the turbulent contributions and the neoclassical contributions of the particle transport fluxes in Eq.(1), we should consider the comparison between both contributions. In our previous work for the neoclassical contributions in the LHD impurity hole plasma transport, if sufficient external torque by the NBI heating exists, the ambi-polar radial electric field can be positive, i.e., the system can be in the electron-root. In this case, the neoclassical particle transport flux of the carbon ion can be radially outward-directed. On the other hand, in the case of the ion-root, the radial electric field is negative, and the neoclassical particle transport flux of the carbon is radially inward-directed. From the results of the nonlinear turbulence simulations performed in the previous subsection, the turbulent contributions of the particle transport flux of the carbon impurity ion should be inward-directed for wide ranges of the radial gradients of the temperatures and densities. Figure 9 shows the comparisons of the particle transport fluxes for each species between the turbulent contributions $\Gamma_s^{(\mathrm{Trb})}$, which are obtained by nonlinear gyrokinetic simulations, and the neoclassical contributions $-\Gamma_s^{(\mathrm{NC})}$, which are obtained by neoclassical simulations performed by utilizing DKES/PENTA code[25,26] in our previous work. If the system is in the ion-root with the negative radial electric field, the neoclassical contributions are absolutely larger than the turbulent contributions, i.e., $|\Gamma_s^{(\mathrm{Trb})}| \ll |\Gamma_s^{(\mathrm{NC})}|$ for electron and bulk ion. On the other hand, if the system is in the electron-root with the positive radial electric field, the neoclassical contributions can be comparable to the turbulent contributions for each species, i.e., $|\Gamma_s^{(\mathrm{Trb})}| \sim |\Gamma_s^{(\mathrm{NC})}|$. In the plot, it is certainly confirmed that the neoclassical particle transport flux of the carbon ion in the electron-root can be slightly radially outward-directed, $\Gamma_{\mathrm{C}}^{(\mathrm{NC})}|_{\text{e-root}} = 2.006\times10^{17}$ [1/m^{2}s], while the flux of the carbon ion in the ion-root is inward-directed, $\Gamma_{\mathrm{C}}^{(\mathrm{NC})}|_{\text{i-root}} = -1.238\times10^{17}$ [1/m^{2}s].

For the different radial position at $\rho = 0.52$ where the impurity hole still remains, the comparisons between the turbulent and the neoclassical particle fluxes are also performed. Figure 10 shows the turbulent and the neoclassical particle fluxes for each species at $\rho = 0.52$ and 0.61. At $\rho = 0.52$, the same as the case of $\rho = 0.61$, the turbulent flux of the carbon ion is still negative, namely, radially inward-directed, and the neoclassical flux of the carbon is radially outward-directed in the case of the electron-root. The inward-directed turbulent particle fluxes of the carbon obtained here are consistent with the previous results in which the quasi-linear particle flux of the carbon impurity are radially inward-directed for different radial positions and for different density gradients in the impurity hole plasma[6]. Furthermore, the turbulent fluxes for electron and hydrogen are the same order of the neoclassical values with opposite signs. For helium ion, the orders match while the direction does not match, which is the same at $\rho = 0.61$. Therefore, if the plasma is in the electron-root, the particle balance relation between the turbulent and the neoclassical contributions may be satisfied at least for main particle species, the electrons and the hydrogen ions. For the carbon ions, since the directions of both contributions matches with quite small fluxes, it may be possible to realize the particle balance relation in the case of the electron-root.

VI. SUMMARY AND DISCUSSIONS

In this work, the first nonlinear gyrokinetic simulations for the turbulent transport of the multi-ion-species helical plasma including impurity carbon ion with the impurity hole structure are carried out. Since the turbulent transport is sensitive to the temperature and the density profiles, we performed many gyrokinetic turbulence simulations for the wide ranges of the radial gradients of the temperatures and the densities. For the turbulent heat transport, due to the typical character of the ITG-driven turbulent transport, all ion heat fluxes rapidly increase with increasing the ion temperature gradient, and the heat fluxes of each species have slightly different dependences on the temperature gradients and the density gra-

dients due to the turbulent potential fluctuation which is shared with all species. Therefore, the turbulent heat transport has slightly different sensitivity on the plasma gradient profiles between each particle species.

For the turbulent particle transport, on the other hand, there are quite different dependences between different particle species on the plasma gradient profiles. On the temperature gradient dependences, if the ion temperature gradient increases, the particle transport fluxes for the hydrogen and the helium ions increase while the particle fluxes of the electron and the carbon ion decrease, and if the electron temperature gradient increases, all particle fluxes decrease, satisfying the ambi-polar condition between different species. For the hydrogen ion, the direction of the particle flux can be changed. Furthermore, the impurity carbon particle flux remains radially inward-directed in wide ranges of the temperature gradients over 50% changes. On the density gradients dependences, there are also quite different dependences between each particle species. In particular, for changing density gradients of bulk ions, there seems to be clear balance relations between the pair of H and He ions and the pair of e and C ion. In addition to the dependences, the carbon turbulent particle flux should not be radially outward-directed unless the impurity hole structure disappears.

The neoclassical particle flux can be changed by the external torques, where the sufficient NBI heating causes the electron-root with positive ambi-polar radial electric field. In the electron-root case with the positive radial electric field, there can be radially outward-directed neoclassical impurity carbon particle flux, and the neoclassical contributions can be comparable to the turbulent contributions. In conclusion, the particle balance relation between the turbulent contributions and the neoclassical contributions may be satisfied in the case of the electron-root at least for main particle species, the electrons, the hydrogen, and the impurity carbon ions.

In this paper, the absolute analyses for the balance relation have not yet been performed, since some physical effects are lacking in the nonlinear gyrokinetic simulations performed here. For example, the simulations employ the model field configuration, and do not include the shearing effects from the radial electric field and the effects of the potential variation on the magnetic surface, i.e., Φ_1 effects[27–29]. Especially, the sheared radial electric field plays a significant role on the reduction of the turbulent transport in LHD with electron internal transport barrier[30] and on the inward pinch of the electron particle transport in JET[31]. Furthermore, the global treatment is also important for the neoclassical analyses, since the global neoclassical estimates by using FORTEC-3D code[32] can give substantial weakening of the neoclassical ion fluxes near the marginal radial electric field $E_r \sim 0$[33,34], which may bring on the outward directed neoclassical impurity particle flux[35]. More precise simulations regarding the issues above will appear elsewhere.

ACKNOWLEDGMENTS

The authors would like to thank the LHD experiment group. This work is supported in part by the Japanese Ministry of Education, Culture, Sports, Science and Technology, Grant (Nos. 18H01202, 19H01879, and 19K03801), by National Institute for Fusion Science (NIFS) Collaborative Research Program (KNST145, KNTT045 and KNTT050), and by the FLAGSHIP2020, MEXT within the priority study 6. The results are obtained by using the K computer at the RIKEN Advanced Institute for Computational Science (Proposal number hp180083), JFRS-1 system at International Fusion Energy Research Center (Project code: KML3D and GDKTHEL), and "Plasma Simulator" of NIFS.

[1] X. Garbet, Y. Idomura, L. Villard, and T.H. Watanabe, Nucl. Fusion **50**, 043002 (2010).
[2] M. Nunami, M. Nakata, S. Toda, A. Ishizawa, R. Kanno, and H. Sugama, Phys. Plasmas **25**, 082504 (2018).
[3] T. Klinger, T. Andreeva, S. Bozhenkov, C. Brandt, R. Burhenn, B. Buttenschön, G. Fuchert, B. Geiger, O. Grulke, H.P. Laqua, *et al.*, Nucl. Fusion **59**, 112004 (2019).
[4] Y. Takeiri, T. Morisaki, M. Osakabe, M. Yokoyama, S. Sakakibara, H. Takahashi, Y. Nakamura, T. Oishi, G. Motojima, S. Murakami, *et al.*, Nucl. Fusion **57**, 102023 (2017).
[5] M. Nunami, M. Nakata, H. Sugama, K. Tanaka, and S. Toda, Plasma Phys. Control. Fusion **59**, 044013 (2017).
[6] D.R. Mikkelsen, K. Tanaka, M. Nunami, T.-H. Watanabe, H. Sugama, M. Yoshinuma, K. Ida, Y. Suzuki, M. Goto, S. Morita, B. Wieland, I. Yamada, R. Yasuhara, T. Tokuzawa, T. Akiyama, and N.A. Pablant, Phys. Plasmas **21**, 082302 (2014).
[7] X. Wei, H. Yang, S. Li, and Y. Xiao, Phys. Plasmas **25**, 082508 (2018).
[8] K. Ida, M. Yoshinuma, M. Osakabe, K. Nagaoka, M. Yokoyama, H. Funaba, C. Suzuki, T. Ido, A. Shimizu, I. Murakami, N. Tamura, H. Kasahara, Y. Takeiri, K. Ikeda, K. Tsumori, O. Kaneko, S. Morita, M. Goto, K. Tanaka, K. Narihara, T. Minami, I. Yamada, and LHD Experimental Group, Phys. Plasmas **16**, 056111 (2009).
[9] M. Nunami, M. Sato, M. Nakata, S. Toda, H. Sugama, M. Yokoyama, and H. Yamaguchi, Plasma Fusion Res. **12**, 1203039 (2017).
[10] T.-H. Watanabe and H. Sugama, Nucl. Fusion **46**, 24 (2006).
[11] M. Nunami, T.-H. Watanabe, and H. Sugama, Plasma Fusion Res. **5**, 016 (2010).
[12] M. Nunami, M. Nakata, T.-H. Watanabe, and H. Sugama, Plasma Fusion Res. **10**, 1403058 (2015).
[13] M. Nakata, M. Nunami, T.-H. Watanabe, and H. Sugama, Comput. Phys. Comm. **197**, 61 (2015).
[14] A. Lenard and I.B. Bernstein, Phys. Rev. **112**, 1456 (1958).
[15] T. Görler, A. E. White, D. Told, F. Jenko, C. Holland and T. L. Rhodes, Phys. Plasmas **21**, 122307 (2014).
[16] A. Ishizawa, T.-H. Watanabe, H. Sugama, M. Nunami, K. Tanaka, S. Maeyama and N. Nakajima, Nucl. Fusion **55**, 043024 (2015).
[17] A. Ishizawa, Y. Kishimoto, T.-H. Watanabe, H. Sugama, K. Tanaka, S. Satake, S. Kobayashi, K. Nagasaki and Y. Nakamura, Nucl. Fusion **57**, 066010 (2017).
[18] A.M. Dimits, G. Bateman, M.A. Beer, B.I. Cohen, W. Dorland, G.W. Hammett, C. Kim, J.E. Kinsey, M. Kotschenreuther, A.H. Kritz, L.L. Lao, J. Mandrekas, W.M. Nevins, S.E. Parker, A.J. Redd, D.E. Shumaker, R. Sydora and J. Weiland, Phys. Plasmas **7**, 969 (2000).
[19] A.M. Dimits, B.I. Cohen, N. Mattor, W.M. Nevins, D.E. Shu-

maker, S.E.=Parker, and C. Kim, Nucl. Fusion **40**, No. 3Y (2000).
[20]C. Holland, A.E. White, G.R. McKee, M.W. Shafer, J. Candy, R.E. Waltz, L. Schmitz, and G.R. Tynan, Phys. Plasmas **16**, 052301 (2009).
[21]T.L. Rhodes, C. Holland, S.P. Smith, A.E. White, K.H. Burrell, J. Candy, J.C. DeBoo, E.J. Doyle, J.C. Hillesheim, J.E. Kinsey, G.R. McKee, D. Mikkelsen, W.A. Peebles, C.C. Petty, R. Prater, S. Parker, Y. Chen, L. Schmitz, G.M. Staebler, R.E. Waltz, G. Wang, Z. Yan and L. Zeng, Nucl. Fusion **51**, 063022 (2011).
[22]C. Holland, Phys. Plasmas **23**, 060901 (2016).
[23]S.P. Hirshman and O. Betancourt, J. Comput. Phys. **96**, 99 (1991).
[24]H. Sugama, M. Okamoto, W. Horton, and M. Wakatani, Phys. Plasmas **3**, 2379 (1996).
[25]D.A. Spong, Phys. Plasmas **12**, 056114 (2005).
[26]H. Sugama, and S. Nishimura, Phys. Plasmas **9**, 4637 (2002).
[27]J.M. García-Regaña, C.D. Beidler, R. Kleiber, P. Helander, A. Mollén, J.A. Alonso, M. Landreman, H. Maaßberg, H.M. Smith, Y. Turkin and J.L. Velasco, Nucl. Fusion **57**, 056004 (2017).
[28]A. Mollén , M. Landreman, H.M. Smith, J.M. García-Regaña and M. Nunami, Plasma Phys. Control. Fusion **60**, 084001 (2018).
[29]K. Fujita, S. Satake, R. Kanno, M. Nunami, M. Nakata, and J.M. García-Regaña, Plasma Fusion Res. **14**, 3403102 (2019).
[30]J. Garcia, K. Yamazaki, J. Dies, and J. Izquierdo, Phys. Rev. Lett. **96**, 105007 (2006).
[31]J. Garcia, H. Doerk, T. Görler, and JET Contributors, Plasma Phys. Control. Fusion **61**, 104002 (2019).
[32]S. Satake, M. Okamoto, N. Nakajima, H. Sugama, and M. Yokoyama, Plasma Fusion Res. **1**, 002 (2006).
[33]B. Huang, S. Satake, R. Kanno, H. Sugama, and S. Matsuoka, Phys. Plasmas **24**, 022503 (2017).
[34]S. Matsuoka, Y. Idomura, and S. Satake, Phys. Plasmas **24**, 102522 (2017).
[35]K. Fujita, S. Satake, R. Kanno, M. Nunami, M. Nakata, J.M. García-Regaña, J.L. Velasco, and I. Calvo, 22nd International Stellarator and Heliotron Workshop 2019.

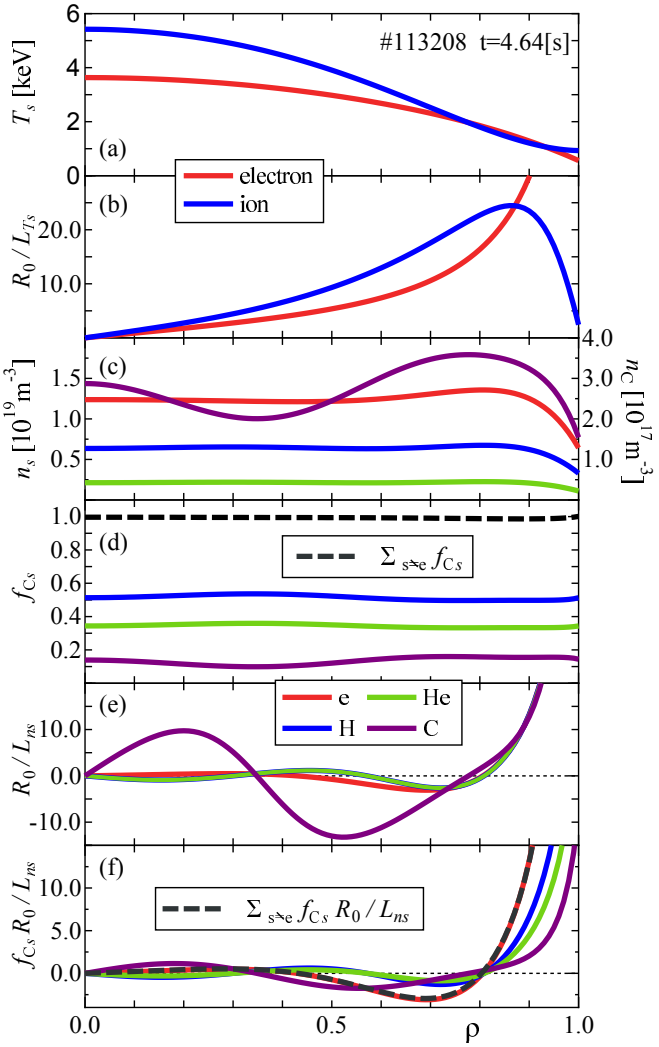

FIG. 1. The radial profiles in the LHD impurity hole plasma #113208 at $t = 4.64$s for (a) the temperatures T_s, (b) the radial gradients of the temperatures R_0/L_{Ts}, (c) the densities n_s, (d) the normalized charge densities f_{Cs}, (e) the radial gradients of the densities R_0/L_{ns}, and (f) $f_{Cs}R_0/L_{ns}$.

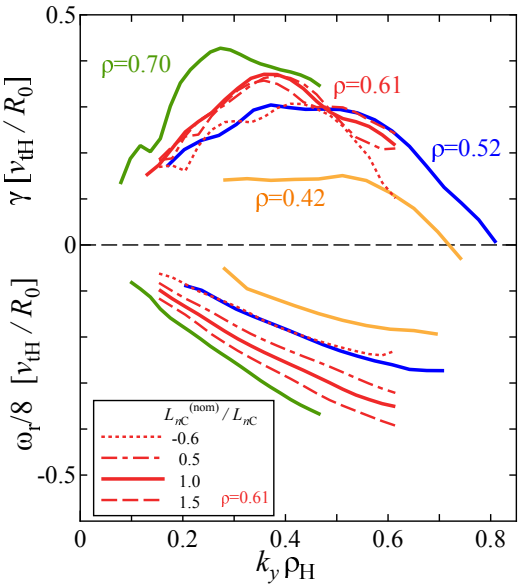

FIG. 2. The growth rates γ and the real frequencies ω_r of the microinstabilities for $\rho = 0.42, 0.52, 0.61$, and 0.70 in the LHD plasma #113208 at $t = 4.64$s. For $\rho = 0.61$, the dotted, dot-dashed, solid, and dashed red curves represent the frequencies for $L_{nC}^{(\mathrm{nom})}/L_{nC} = -0.6, 0.5, 1.0$, and 1.5, respectively.

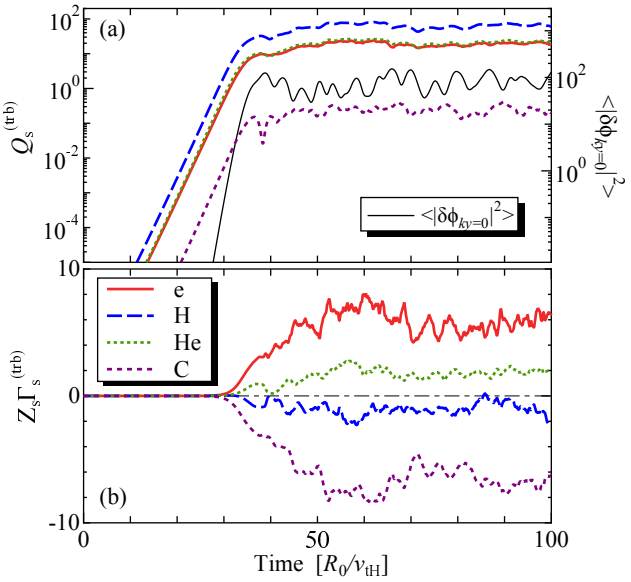

FIG. 3. The time evolutions of (a) the turbulent heat fluxes $Q_s^{(\mathrm{Trb})}$ and (b) the turbulent particle fluxes $Z_s\Gamma_s^{(\mathrm{Trb})}$ for each species with the nominal parameters of the plasma profiles. $Q_s^{(\mathrm{Trb})}$ is normalized by $\rho_{\mathrm{H}}^2 v_{\mathrm{tH}} T_{\mathrm{i}}(\rho) n_{\mathrm{e}}(\rho)/R_0^2$, and $Z_s\Gamma_s^{(\mathrm{Trb})}$ is normalized by $\rho_{\mathrm{H}}^2 v_{\mathrm{tH}} n_{\mathrm{e}}(\rho)/R_0^2$. In (a), the black solid curve represents the time evolution of the zonal flow component of the potential fluctuation $\langle|\delta\phi_{ky=0}|^2\rangle$.

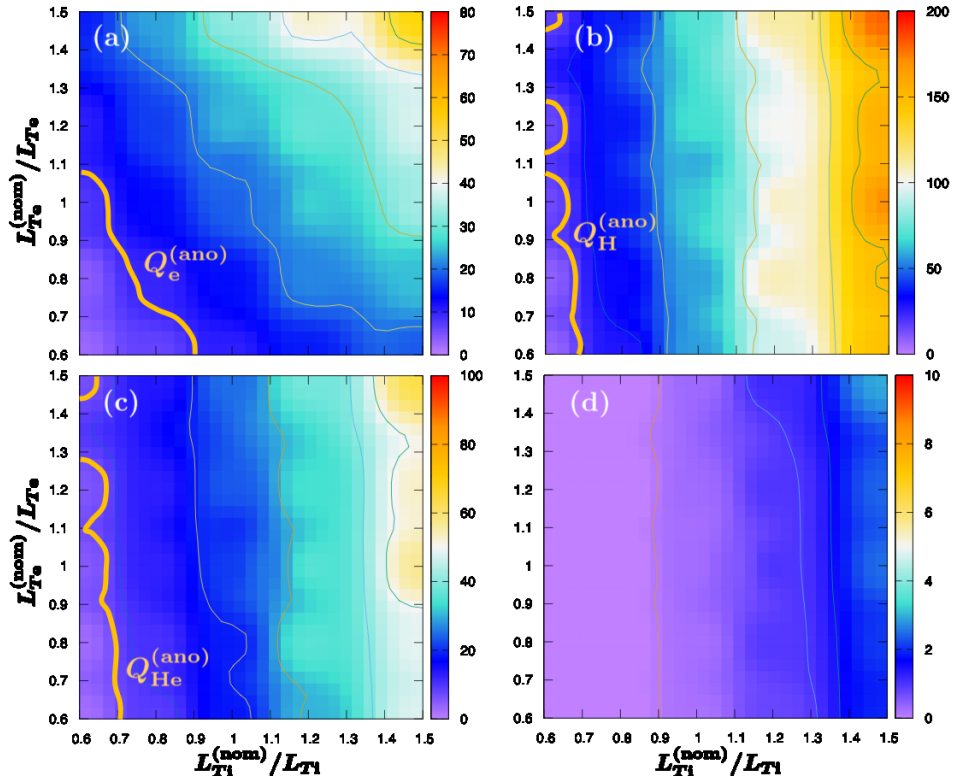

FIG. 4. Temperature gradient length dependences of turbulent heat fluxes $Q_s^{(\mathrm{Trb})}$ (color contours) for (a) electron, (b) hydrogen, (c) helium, and (d) carbon, where $L_{T\mathrm{e}}^{(\mathrm{nom})}$ and $L_{T\mathrm{i}}^{(\mathrm{nom})}$ represent the nominal temperature gradient lengths for electron and all ion species, respectively. Each flux is evaluated at $\rho = 0.61$ and normalized by the same unit, $\rho_{\mathrm{H}}^2 v_{\mathrm{tH}} T_{\mathrm{i}}(\rho) n_{\mathrm{e}}(\rho)/R_0^2$. In (a), (b), and (c), the bold curves represent the experimental values of the anomalous contributions of the heat fluxes $Q_s^{(\mathrm{ano})}$ for $s = \mathrm{e},\ \mathrm{H},$ and He, respectively.

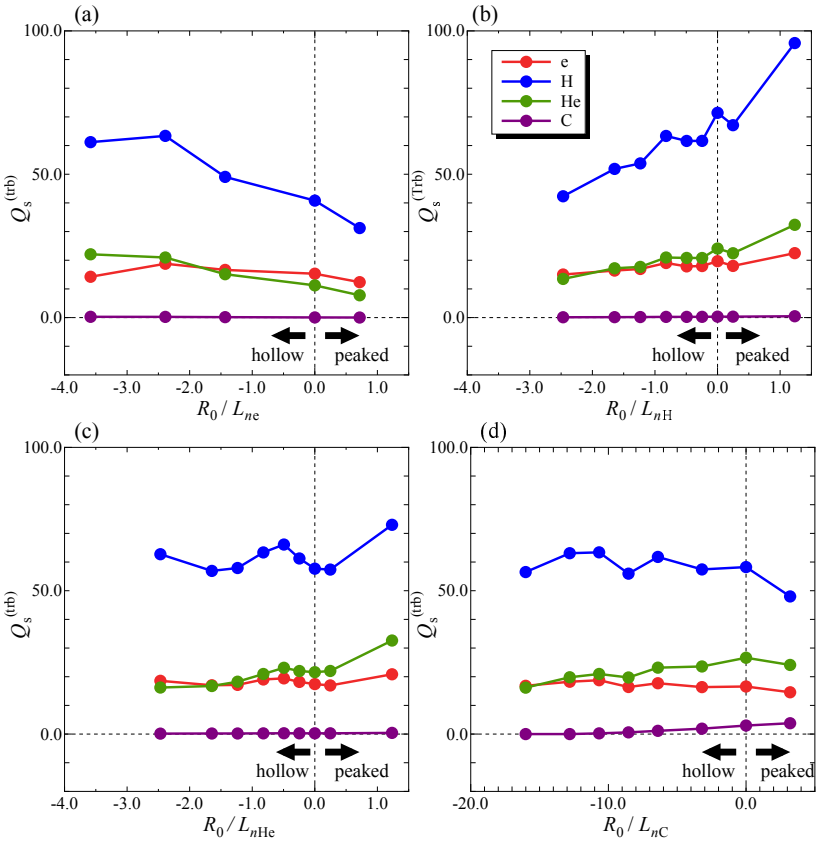

FIG. 5. Density gradient length dependences of turbulent heat fluxes $Q_s^{(\mathrm{Trb})}$ for (a) electron density gradients, (b) hydrogen density gradients, (c) helium density gradients, and (d) carbon density gradients. Each flux is evaluated at $\rho = 0.61$ and normalized by the same unit, $\rho_{\mathrm{H}}^2 v_{\mathrm{tH}} T_{\mathrm{i}}(\rho) n_{\mathrm{e}}(\rho) / R_0^2$.

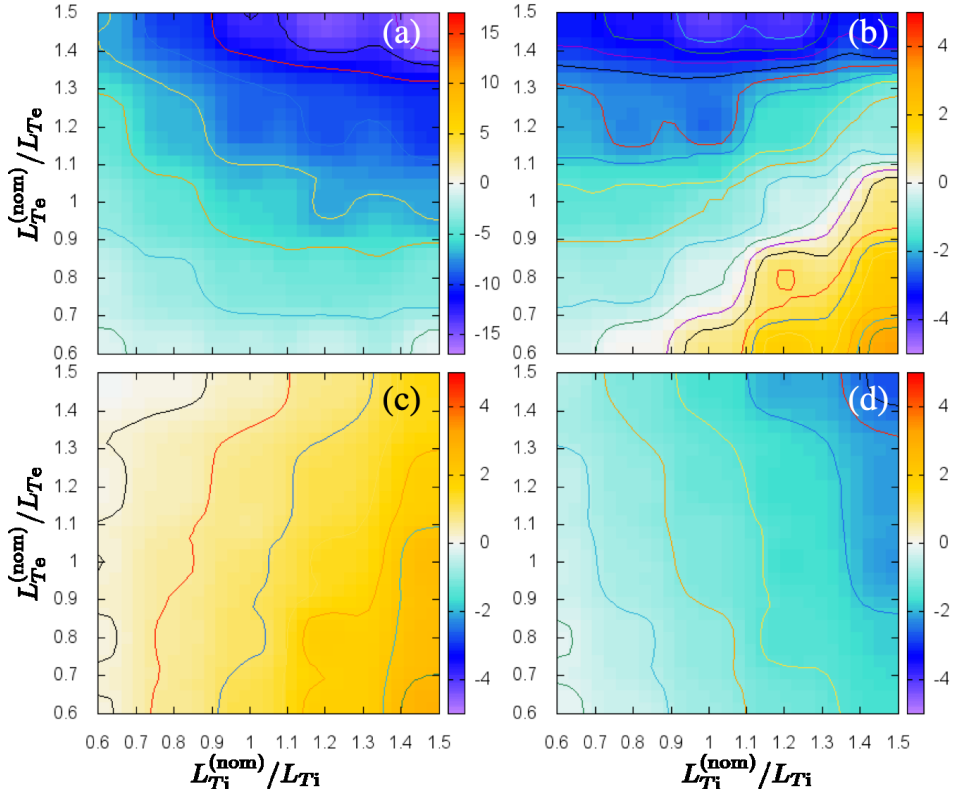

FIG. 6. Temperature gradient length dependences of turbulent particle fluxes $\Gamma_s^{(\mathrm{Trb})}$ (color contours) for (a) electron, (b) hydrogen, (c) helium, and (d) carbon, where $L_{Te}^{(\mathrm{nom})}$ and $L_{Ti}^{(\mathrm{nom})}$ represent the nominal temperature gradient lengths for electron and all ion species, respectively. Each flux is evaluated at $\rho = 0.61$ and normalized by the same unit, $\rho_{\mathrm{H}}^2 v_{\mathrm{tH}} n_{\mathrm{e}}(\rho)/R_0^2$.

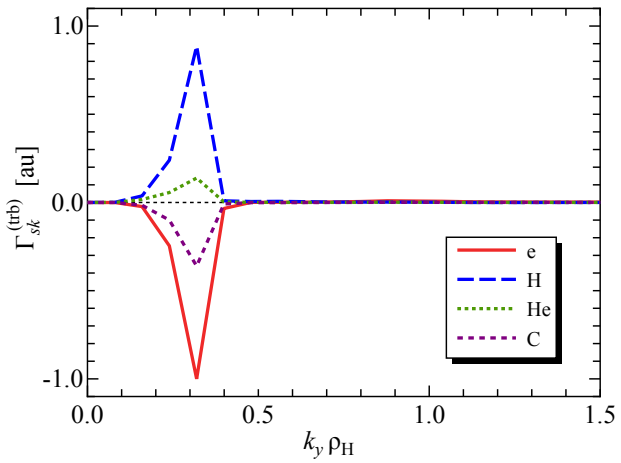

FIG. 7. The wavenumber spectra of the particle fluxes for each particle species in the case of $L_{Ti}^{(\mathrm{nom})}/L_{Ti} = 1.5$ at $\rho = 0.61$.

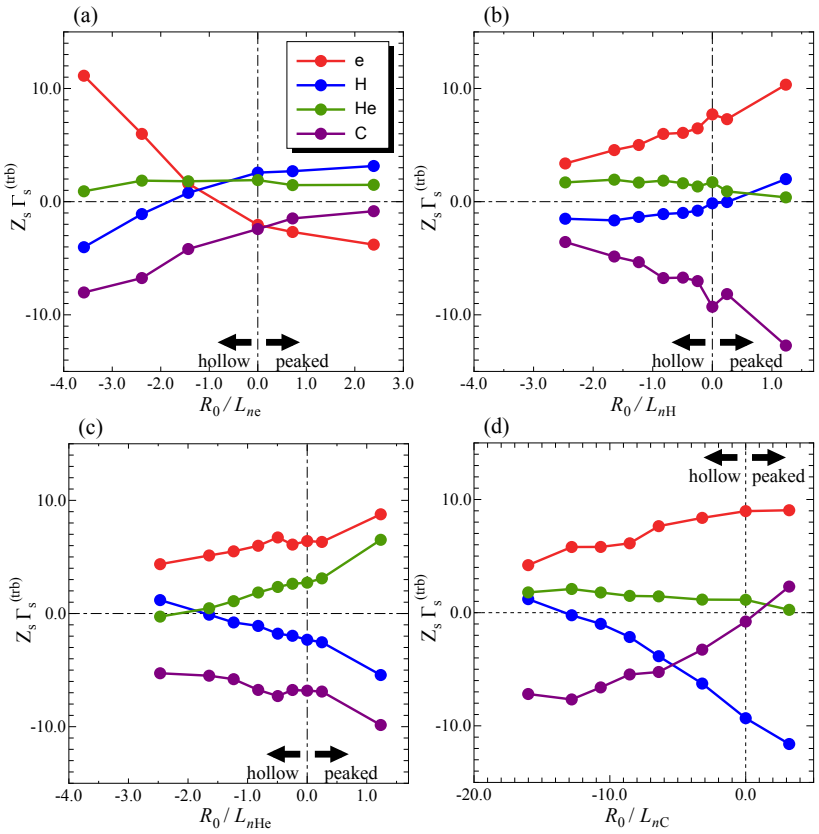

FIG. 8. Density gradient dependences of turbulent particle fluxes $Z_s\Gamma_s^{(\mathrm{Trb})}$ for (a) electron density gradients, (b) hydrogen density gradients, (c) helium density gradients, and (d) carbon density gradients. Each flux is evaluated at $\rho = 0.61$ and normalized by the same unit, $\rho_{\mathrm{H}}^2 v_{\mathrm{tH}} n_{\mathrm{e}}(\rho)/R_0^2$.

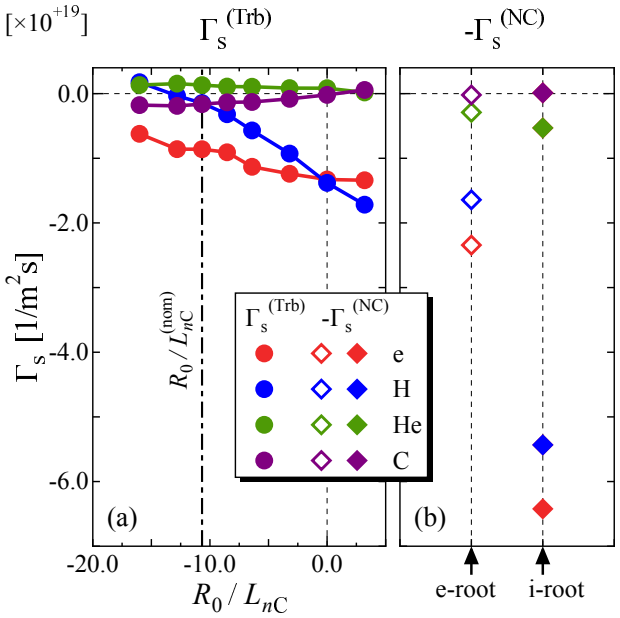

FIG. 9. Comparisons between (a) the turbulent contributions $\Gamma_s^{(\mathrm{Trb})}$ and (b) the neoclassical contributions with opposite sign $-\Gamma_s^{(\mathrm{NC})}$ of the particle transport fluxes for each particle species. For the neoclassical contributions, the filled diamonds show the particle fluxes in the case of ion-root, and the open diamonds show the fluxes in the case of electron-root.

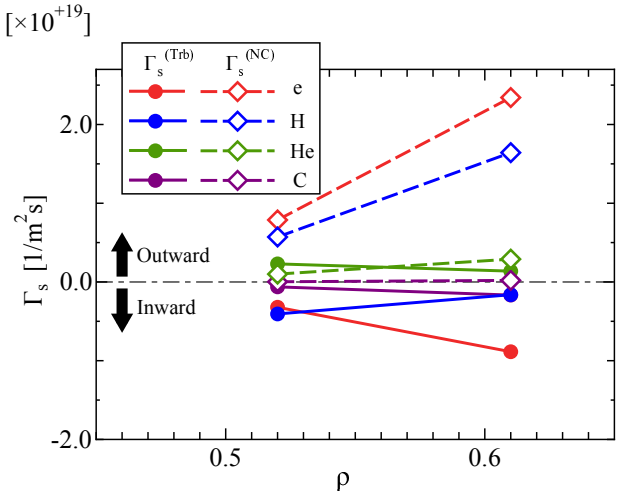

FIG. 10. The turbulent and the neoclassical particle fluxes for each species at $\rho = 0.52$ and 0.61. The neoclassical fluxes are evaluated in the case of electron-root.